

Material-dependent backscatter formation in gamma-ray spectra: a transparent Monte Carlo approach

M. Perdomo-Gutiérrez and J. Prada-Suarez
(Dated: December 2, 2025)

This work presents GammaSpectra-MC, a lightweight hybrid C++/Python Monte Carlo engine designed to reproduce gamma-ray spectra in laboratory geometries. The framework combines analytical ray–geometry navigation, faithful Klein–Nishina sampling, and an experimentally calibrated detector response to model the formation of low-energy continua and backscatter peaks. Comparisons with spectra from four standard radioactive sources (^{137}Cs , ^{54}Mn , ^{133}Ba , ^{88}Y) show excellent agreement, with copper and lead simulations bounding the data according to their atomic numbers. The results confirm that backscatter formation is driven by large-angle Compton interactions in low- Z materials and validate the transport scheme across a range of emission and geometric conditions. GammaSpectra-MC provides a transparent and efficient tool for spectral modeling and hypothesis-driven studies in radiation detection.

Keywords: Monte Carlo simulation; gamma-ray spectra; Compton scattering; backscatter peak; Klein–Nishina sampling; CsI(Tl) detectors; radiation transport; shielding materials.

I. INTRODUCTION

Accurate characterization of the gamma-ray spectral response functions is essential in experimental nuclear physics, medical dosimetry, and non-destructive industrial testing [1]. Although the primary photon–matter interaction mechanisms—photoelectric absorption, Compton scattering, and pair production—are described by well-established physical laws [2], the resulting measured spectrum is strongly influenced by the detector environment. Intrinsic features such as the photopeak can often be modeled analytically, whereas extrinsic components depend sensitively on the surrounding materials and geometry.

Among these extrinsic components, the backscatter peak remains one of the most challenging to model. Originating from photons that undergo large-angle scattering in external structures before re-entering the detector, this feature cannot be fully captured by analytical approaches. As shown by Hie [3], the centroid energy of the backscatter peak can be estimated from the incident photon energy E_0 and the Compton edge E_c via $E_{\text{BS}} \approx E_0 - E_c$; however, the lineshape—its width, asymmetry, and relative intensity—cannot be expressed in a closed form. These parameters are highly dependent on the specific scattering environment and are typically obtained empirically.

Consequently, a predictive understanding of backscatter phenomena requires Monte Carlo (MC) transport simulations capable of modeling complex geometries and multiple scattering effects. Extensive research demonstrates the necessity of MC methods when analytical treatments break down because of material heterogeneity or nonlinear accumulation of scattered photons. For instance, Flechas et al. [4, 5] used GEANT4 [6, 7] to show that imaging techniques based on Compton backscattering rely critically on simulation to interpret

non-analytical spectral and spatial distributions. In industrial applications, Wirawan et al. [8] demonstrated that backscatter intensity correlates with crack width in aluminum alloys, while Iori and Boldo [9] used FLUKA to investigate rebar detection in reinforced concrete, highlighting the sensitivity of backscatter to the effective atomic number Z of the medium. Medical physics provides further evidence: Ryczkowski et al. [10] recently showed that shielding materials significantly alter the backscattered dose distribution in intraoperative radiotherapy, with low- Z materials offering reduced undesired scatter.

Other modern studies corroborate these dependencies. Aydin [11] analyzed the energy distributions of multiply backscattered photons in various materials, demonstrating that the spectral contribution of higher-order Compton events depends systematically on thickness and Z . Similarly, Akar Tarim et al. [12] modeled single and multiple Compton scattering profiles in concrete, showing the degradation of the spectral peaks with increasing material depth. Zuo et al. [13] further confirmed strong material-dependent reflection effects using a dedicated MC framework, while Nikrah et al. [14] reported significant modifications in backscattered spectra when nanoparticle-enhanced shielding layers are introduced.

Despite the robustness of well-established toolkits such as GEANT4 and MCNP, their architectural complexity often hinders fine-grained control over specific physical processes or geometric configurations. For educational, exploratory, or hypothesis-testing scenarios, a transparent computational engine—with easily modifiable physics options and explicit control of detector and shielding geometry—is highly advantageous.

This work introduces GammaSpectra-MC, a hybrid (C++/Python) Monte Carlo transport engine designed

to provide such transparency. The engine implements analytical ray-tracing for photon transport in canonical laboratory geometries (notably the Canberra Model 747 lead shield) while enabling full control over material composition and geometry at runtime. By simulating a variety of laboratory sources (^{137}Cs , ^{54}Mn , ^{133}Ba , ^{88}Y) in both high- Z (lead) and low- Z (copper) environments, this study demonstrates that the dominant contribution to the experimentally observed backscatter peak originates from scattering in light structural materials surrounding the detector—consistent with the material-dependent trends reported in recent literature [10, 11, 13, 14].

II. THEORETICAL AND COMPUTATIONAL FRAMEWORK

The GammaSpectra-MC engine implements a semi-classical photon transport model designed for the energy domain typical of laboratory gamma-ray sources (from a few hundred keV up to several MeV). Particular emphasis is placed on the low-energy region ($E_{\text{BS}} \lesssim 300$ keV) where backscatter features arise after multiple large-angle Compton scattering events in surrounding materials. Unlike general-purpose Monte Carlo toolkits—which rely on complex voxel-based navigation and layered physics lists—GammaSpectra-MC employs analytical ray-tracing in idealized geometries and a transparent modular architecture. This approach enables explicit control over each physical interaction and material component, facilitating isolated studies of geometric contributions to the backscatter peak.

A. Physical interaction model

Photon transport in the energy range of interest is governed primarily by photoelectric absorption and Compton scattering. These processes determine the shape of the detected spectrum and, in particular, the structure of the backscatter peak [1, 2, 15]. Pair production is excluded in the present configuration because its contribution to sub-MeV spectral features is negligible for the isotopes studied; however, the physics engine is fully modular and allows its inclusion for higher-energy applications.

Macroscopic attenuation and free-flight sampling

The interaction probability in a material is characterized by the macroscopic attenuation coefficient,

$$\Sigma(E) = \rho \mu_m(E), \quad (1)$$

where ρ is the mass density and $\mu_m(E)$ is the mass attenuation coefficient obtained from the NIST/XCOM database [16]. To avoid discretization artifacts, $\mu_m(E)$ is interpolated in log-log space within the C++ backend, ensuring smooth behavior over the continuous energy domain sampled by Compton scattering.

The photon mean free path is given by

$$\lambda(E) = \frac{1}{\Sigma(E)}, \quad (2)$$

and the stochastic distance to the next interaction is sampled using the exponential survival law,

$$s = -\lambda(E) \ln(\xi), \quad \xi \sim U(0, 1). \quad (3)$$

At the interaction site, the process type is selected according to the relative contributions of the partial macroscopic cross sections

$$P(\text{Compton}|E) = \frac{\Sigma_{\text{C}}(E)}{\Sigma(E)}, \quad P(\text{Photoelec}|E) = \frac{\Sigma_{\text{PE}}(E)}{\Sigma(E)}.$$

Compton scattering

Compton scattering is the dominant mechanism responsible for generating backscattered photons. The differential cross section per electron is given by the Klein–Nishina formula

$$\frac{d\sigma}{d\Omega}(\theta; E_0) = \frac{r_e^2}{2} \left(\frac{E'}{E_0} \right)^2 \left[\frac{E'}{E_0} + \frac{E_0}{E'} - \sin^2 \theta \right], \quad (4)$$

where E_0 and E' are the incident and scattered photon energies, θ is the scattering angle, and r_e is the classical electron radius [15, 17]. The scattered energy is

$$E' = \frac{E_0}{1 + \frac{E_0}{m_e c^2} (1 - \cos \theta)}. \quad (5)$$

Sampling of θ from Eq. (4) is performed using a dedicated rejection-sampling algorithm optimized for high-energy tail suppression and numerical stability.

The post-scattering direction is obtained by constructing a local orthonormal basis around the incident direction and applying Rodrigues' rotation formula [18, 19]. This avoids the gimbal-lock singularity inherent in Euler-angle parameterizations and ensures stable multi-scatter trajectories—an essential requirement for correctly modeling backscattered photons that undergo multiple large-angle interactions before reaching the detector.

Photoelectric absorption

Photoelectric interactions are treated as terminal events since they result in complete removal of the photon from the transport chain. Because secondary electrons are not tracked in the present model, full photon energy at the interaction site is assumed to be deposited locally [1].

B. Transport algorithm

The transport algorithm advances particles through alternating free-flight and interaction phases, following the standard Monte Carlo radiation transport paradigm [1, 20]. The stochastic transport relies on a “delta-tracking” approach adapted for analytical geometries, utilizing boundary navigation strategies inspired by standard analytical tracking methods found in toolkits such as GEANT4 [6]. The life cycle of a single photon history proceeds through the following steps.

- 1. Initialization:** A photon is generated with energy E_0 sampled from the characteristic emission lines and branching ratios of the target isotope, obtained from the NuDat database [21] (e.g., 661.66 keV for ^{137}Cs). The initial position \mathbf{r} and direction \mathbf{d} are sampled according to the selected source configuration (e.g., isotropic point source).

- 2. Step Calculation:** Two distances are computed to determine the next event.

- (a) t_{int} : Distance to the next physical interaction, sampled via Eq. (3).
- (b) t_{bnd} : Distance to the nearest geometric boundary along \mathbf{d} .

The actual step size is defined as $t = \min(t_{\text{int}}, t_{\text{bnd}})$.

- 3. Streaming:** The photon is propagated to $\mathbf{r}' = \mathbf{r} + t\mathbf{d}$.

- (a) If $t_{\text{bnd}} < t_{\text{int}}$ (*Cross Region*): The photon crosses a boundary. The material index is updated, and the particle continues without interaction.
- (b) If $t_{\text{int}} < t_{\text{bnd}}$ (*Interaction*): An interaction occurs. The type is sampled based on partial cross sections.

- 4. Interaction & Scoring**

- (a) *Photoelectric*: The photon is absorbed. If the event occurs within the active detector volume, the full photon energy E is deposited [1]. The history ends.
- (b) *Compton*: A new direction \mathbf{d}' and energy E' are sampled using Eq. (4), based on the Klein-Nishina distribution [17]. If the interaction occurs inside the detector, the deposited energy is $E_{\text{dep}} = E - E'$. The photon continues with energy E' and direction \mathbf{d}' .

- 5. Termination:** The history ends when the photon is absorbed, escapes the world volume, or its energy falls below the cutoff ($E_{\text{min}} = 1$ keV).

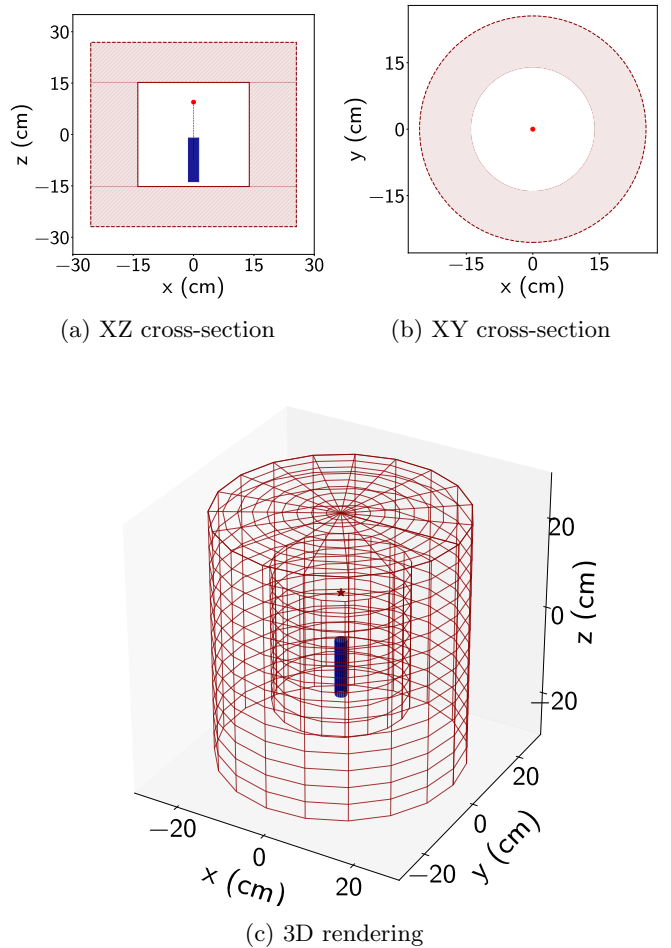


FIG. 1: Geometrical model of the simulated setup, including axial and transverse cross-sections and a 3D visualization of the detector and shielding assembly.

C. Geometrical model and materials

The simulated geometry reproduces the experimental arrangement used in the Nuclear Physics Group of the Universidad Nacional de Colombia. The setup corresponds to a Canberra Model 747 annular shield containing a cylindrical CsI(Tl) scintillation detector (1×5 inches), placed coaxially with respect to the gamma source. The detector position, source-detector separation, and shield boundaries follow the measured laboratory configuration, while Fig. 1 provides the relevant axial and transverse projections as well as a 3D rendering of the complete assembly.

Although the physical shield includes an internal copper lining and an external lead layer, the simulations treat the shielding as a single homogeneous material. This choice allows controlled comparisons between high- Z (Pb) and low- Z (Cu) environments while preserving identical geometric conditions. All void regions are modeled as vacuum to isolate the effects of solid materials on the backscattered photon population.

Detector resolution model

To incorporate the intrinsic energy resolution of the CsI(Tl) detector, each simulated energy deposit is convolved with a Gaussian response function whose width follows

$$\text{FWHM}(E) = a\sqrt{E} + bE. \quad (6)$$

The empirical parameters (a, b) were obtained from calibration measurements performed by the authors, using Gaussian fits to the characteristic gamma-ray lines of standard laboratory sources such as Cs-137, Na-22, Y-88, Co-60, and Mn-54. These spectra were independently energy-calibrated prior to extracting the resolution curve, which is shown in Fig. 2. This convolution broadens both the Compton continuum and the backscatter peak, ensuring consistency between simulated and measured spectra.

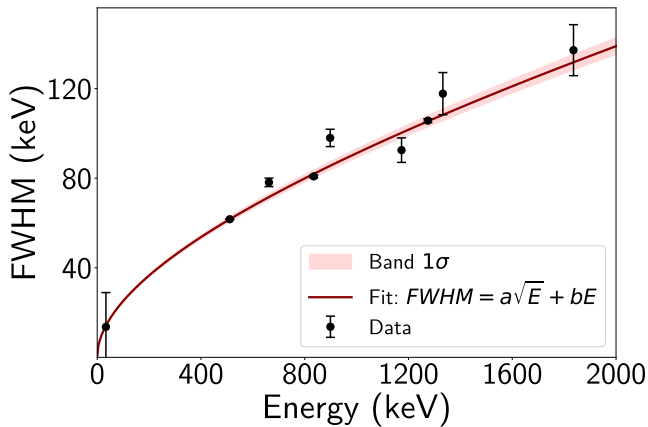


FIG. 2: Measured CsI(Tl) energy resolution (FWHM) used to convolve simulated spectra.

Although the present study focuses on a 1×5 inch CsI(Tl) crystal, the computational model is detector-agnostic: any cylindrical scintillator or semiconductor detector can be simulated by modifying its geometric parameters and supplying the appropriate energy-resolution calibration (i.e., the coefficients a and b of the FWHM model). This flexibility allows GammaSpectra-MC to be readily adapted to NaI(Tl), LaBr₃, HPGe, or other detection systems without altering the underlying transport physics.

D. Software architecture

The GammaSpectra-MC engine follows a hybrid C++/Python design that maximizes performance while maintaining transparency of the underlying physics. Because the experimental setup consists solely of coaxial cylindrical bodies, the code employs analytical ray–geometry intersection tests instead of voxel navigation, reducing computational overhead and enabling fast, exact boundary tracking.

At the core of the system lies a *C++17* backend responsible for all computationally intensive components: (i) log–log interpolation of NIST/XCOM attenuation coefficients, (ii) exact sampling of Compton scattering via the Klein–Nishina differential cross section [17], (iii) photoelectric interaction handling, and (iv) geometric navigation through closed-form ray–cylinder intersection tests. These modules are implemented through dedicated classes such as `PhysicsEngine`, `KleinNishinaExact`, `VectorRotator`, and `GeometryNavigator`, each encapsulating a distinct element of the transport kernel.

The Python layer provides the high-level workflow: initializing C++ modules, selecting sources and materials, running transport batches, and performing spectral post-processing. While many simulation parameters can be modified from Python, changes to core geometric definitions are carried out in the C++ geometry module to retain consistency with the analytical navigation scheme.

Lightweight *PyBind11* bindings [22] connect both layers without unnecessary data copies, preserving C++ performance while allowing Python-based orchestration. Simulations with $\mathcal{O}(10^7)$ photons already yield statistically stable spectra, and the engine achieves a throughput of $\sim 2 \times 10^4$ photon histories per second on standard hardware (Google Colab).

Overall, the architecture provides a clear and auditable transport pipeline—rather than a general-purpose simulation toolkit—allowing individual physical and geometric contributions to be isolated explicitly. This separation between the C++ physics core and the Python steering layer ensures deterministic transport behavior and supports systematic studies of backscatter formation under controlled modifications of geometry and materials.

E. Simulation parameters

All simulations were performed using 2×10^7 photon histories per isotope, with a fixed random seed to ensure reproducibility, a value chosen as an optimal compromise between achieving statistically stable backscatter spectra and maintaining feasible execution times on standard hardware. Initial photon energies were sampled from the emission probabilities and branching ratios listed in the NuDat database [21], while the source was treated as a point-like emitter. Two shielding configurations—copper and lead—were simulated under identical geometric conditions to isolate the influence of material composition on the backscattered component.

A photon was classified as backscattered when it underwent at least one Compton interaction inside the shielding material and subsequently entered the active volume of the detector, depositing part or all of its remaining energy. This criterion, implemented through explicit tracking of material crossings, ensures that

only photons genuinely originating from the external environment contribute to the backscatter spectrum.

In addition to the physical isotropic emission model, two alternative directional sampling modes were used for diagnostic purposes. The hemispherical mode restricts emission to directions pointing toward the detector, improving sampling efficiency without altering the underlying transport physics. The axial mode forces all photons to begin with direction $-z$, i.e. directly downward along the detector axis shown in Fig. 1 (a), and is employed solely for geometric debugging. After transport, each energy deposition was convolved with the experimental resolution function Fig. 2, and the resulting spectra—including the isolated backscatter component—were exported in CSV format for direct comparison with measured data.

III. RESULTS AND DISCUSSION

The analysis begins with the ^{137}Cs spectrum, which highlights an important methodological point. Fig. 3 compares the experimentally measured spectrum with normalized simulations obtained assuming pure copper and pure lead shielding. In this particular case, the normalization behaves reasonably well because the maximum count rate always occurs at the X-ray peak, producing a visually stable reference across all spectra. However, normalization is not well suited for comparing the absolute height of backscatter peaks, which depend sensitively on shielding composition and cannot be meaningfully rescaled without distorting their relative magnitude. For this reason, all remaining spectra in this section are presented without normalization.

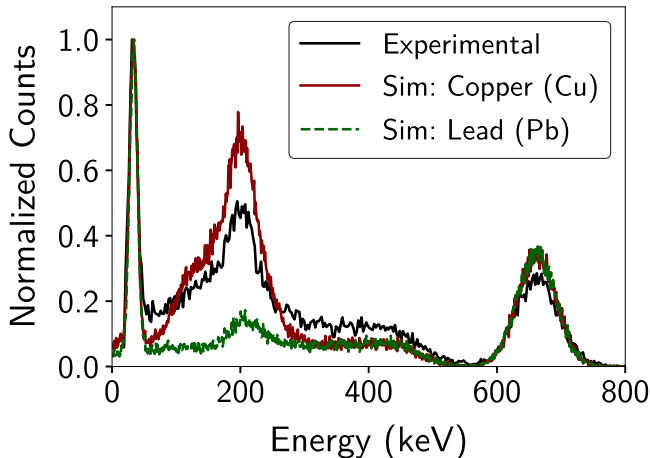


FIG. 3: Normalized experimental and simulated spectra for ^{137}Cs .

Figures 4–6 show the full non-normalized comparisons for the four isotopes investigated. Across all cases, the simulations with copper consistently exhibit a more

pronounced backscatter contribution, as expected from the lower atomic number of copper, which enhances Compton scattering relative to photoelectric absorption. Lead, in contrast, suppresses large-angle scattering and produces a much weaker backscatter component.

The behavior across isotopes reflects their differing spectral characteristics. For ^{133}Ba (Fig. 5), the multi-line structure introduces additional sensitivity to scattering depth and detector resolution, making agreement in the low-energy region a stringent test of the model. For ^{88}Y (Fig. 4), whose emissions extend into the MeV range, the divergence between copper and lead appears most clearly in the high-energy Compton continuum, following expectations from the underlying cross-section systematics.

In all cases, the experimental backscatter peak lies between the copper and lead predictions, consistent with the composite Cu+Pb shielding of the real setup. This bracketing behavior, already visible in the ^{137}Cs comparison (Fig. 3), confirms not only the material dependence of backscatter formation but also the correct sampling of the Klein–Nishina angular distribution implemented in the transport kernel, which had been independently validated in earlier development tests.

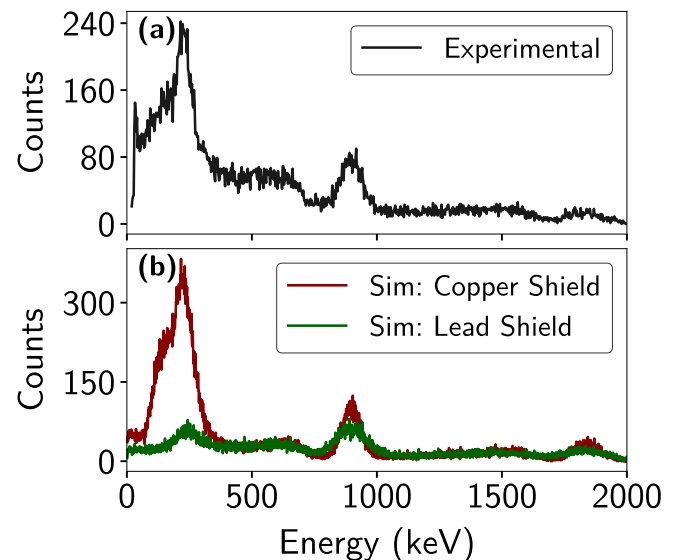


FIG. 4: Experimental and simulated gamma-ray spectra for ^{88}Y . Panel (a) shows the measured spectrum; panel (b) compares simulations with copper and lead shielding.

The isolated backscatter spectra, extracted according to the criterion described in Sec. II E and shown in Fig. 7, reveal clear material-dependent features that are not immediately apparent in the full spectra. In the case of ^{137}Cs , the copper simulation exhibits a noticeably more complex structure: the backscatter maximum develops a pronounced left-hand shoulder that is also present in the experimental data, whereas

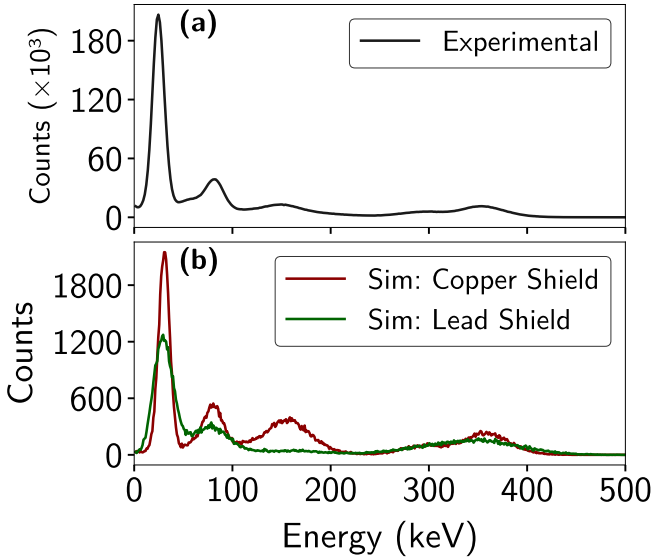


FIG. 5: Experimental and simulated gamma-ray spectra for ^{133}Ba . Panel (a) shows the measured spectrum; panel (b) compares simulations with copper and lead shielding.

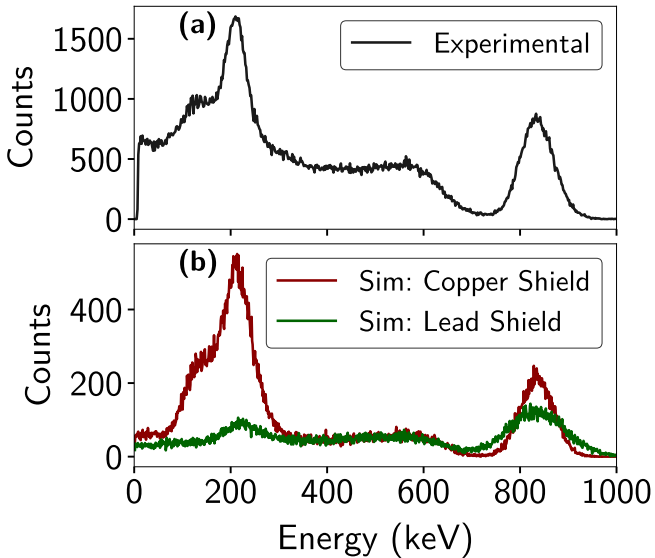


FIG. 6: Experimental and simulated gamma-ray spectra for ^{54}Mn . Panel (a) shows the measured spectrum; panel (b) compares simulations with copper and lead shielding.

the lead simulation produces a much simpler, narrower peak. This asymmetry reflects the enhanced probability of large-angle Compton scattering in low- Z materials.

For ^{133}Ba , the effect is even more striking. Owing to its multi-line emission structure, the backscatter distribution becomes intrinsically composite, giving rise to a wider and more intricate profile whose detailed shape

plays a significant role in reproducing the measured spectrum (see Fig. 5).

For the ^{137}Cs case, Fig. 7 also includes a vertical line marking the theoretical position of the backscatter peak obtained from Eq. (5). Interestingly, both the simulated and theoretical maxima appear slightly shifted to the right relative to the naive expectation based solely on 180° Compton scattering. This subtle displacement has been reported in the literature and is typically attributed to angular averaging effects and the contribution of multiply scattered photons [1, 2].

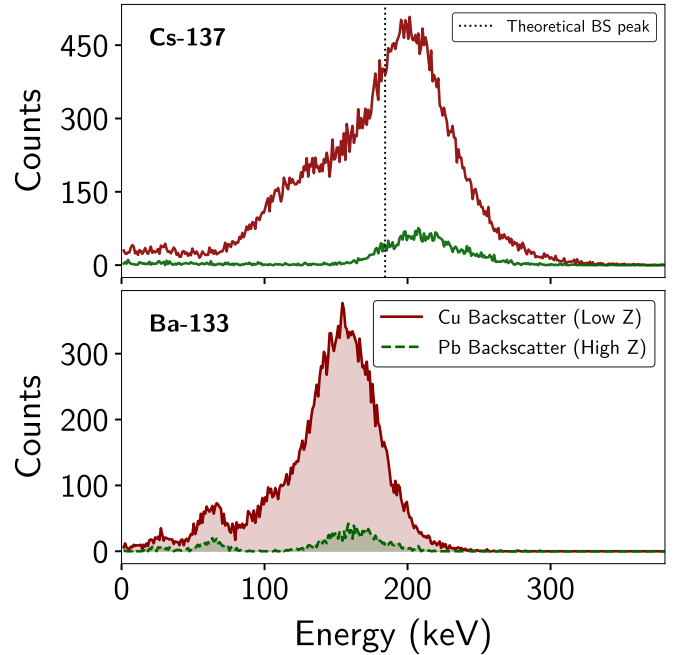


FIG. 7: Isolated backscatter spectra for ^{137}Cs and ^{133}Ba , comparing simulations with copper and lead shielding.

Beyond the spectral comparisons, Table I quantifies the overall detection efficiency and the number of backscatter-classified events for all isotopes under both shielding configurations. A clear and systematic trend emerges: copper, owing to its lower atomic number, produces substantially more large-angle Compton interactions than lead. As a consequence, the detection efficiency approximately doubles when replacing Pb with Cu, and the number of backscattered photons increases by more than an order of magnitude in several cases (notably ^{54}Mn and ^{137}Cs).

Finally, to assess the sensitivity of the transport kernel to the initial directional sampling of the source, the three emission modes described in Sec. II E were evaluated for the ^{137}Cs source under copper shielding: full isotropy (iso), downward hemisphere (hemi), and axial emission (fixed). The resulting spectra and detection statistics are summarized in Table II.

Source	Shield	Detected	Efficiency (%)	BS events
^{137}Cs	Pb	56 745	0.28	4 232
^{137}Cs	Cu	101 863	0.51	49 279
^{133}Ba	Pb	67 456	0.34	1 836
^{133}Ba	Cu	89 702	0.45	23 985
^{54}Mn	Pb	51 422	0.26	4 956
^{54}Mn	Cu	102 060	0.51	55 635
^{88}Y	Pb	46 618	0.23	4 505
^{88}Y	Cu	90 763	0.45	48 831

TABLE I: Detection efficiency and backscatter counts for all isotopes. Each simulation used 2×10^7 emitted photons.

The isotropic and hemispherical modes produce nearly identical spectral shapes once normalized, confirming that the backscatter component is dominated by photons that reach the shielding at large angles, largely independent of the initial emission bias. The hemispherical mode, however, increases the detected rate by a factor of ~ 2 due to the suppression of upward-going photons, which have a low probability of reaching the detector in the event that they undergo Compton interactions within the shielding.

The fixed $-z$ configuration behaves very differently. Because *all* photons are forced directly toward the detector axis, the detection efficiency approaches unity: essentially every photon enters the detector at least once. Despite this dramatic increase in detected events, the number of photons classified as backscattered is actually *lower* than in the isotropic or hemispherical modes (Table II). This reflects the fact that, under such an artificial and highly collimated input distribution, very few photons intercept the shielding with the large angles required to generate a well-defined backscatter peak. As a result, the backscatter component becomes suppressed and distorted, and no clear backscatter structure emerges—even in a low- Z environment such as copper.

For these reasons, the fixed mode serves primarily as a geometric debugging tool, allowing validation of boundary handling and interaction sequencing under extreme and physically unrealistic conditions.

Mode	Detected	Eff. (%)	BS events
iso	101 863	0.51	49 279
hemi	178 040	0.89	73 669
fixed	19 770 307	98.85	47 375

TABLE II: ^{137}Cs statistics under different emission modes (Cu shielding).

Taken together, the results presented in this section demonstrate that the hybrid transport framework accurately reproduces the dominant mechanisms that shape

low-energy continua and backscatter features in gamma-ray spectra. The consistent bracketing of experimental data between copper and lead simulations validates both the material modeling and the implementation of the interaction physics, while the isolated backscatter extractions reveal subtle structural details that are otherwise obscured in the full spectra. Furthermore, the controlled variation of emission modes confirms the robustness of the model to changes in the source’s angular sampling and highlights the physical conditions under which backscatter formation is either enhanced or suppressed. Overall, the combination of spectral agreement, statistical consistency, and physically interpretable trends provides strong evidence that the simulation captures the essential transport dynamics governing the experimental configuration.

IV. CONCLUSIONS

This work presented GammaSpectra-MC, a hybrid C++/Python Monte Carlo engine designed to reproduce laboratory gamma-ray spectra under controlled geometric and material configurations. By combining analytical ray-geometry navigation with a faithful Klein–Nishina sampling algorithm based on rejection techniques, together with an experimentally calibrated detector response, the framework captures the dominant mechanisms that shape low-energy continua and backscatter features in CsI(Tl) detectors.

Comparative simulations using copper and lead shielding exhibited a clear and consistent bracketing of the measured spectra for all isotopes studied (^{137}Cs , ^{54}Mn , ^{133}Ba , and ^{88}Y). This behavior demonstrates that the experimentally observed backscatter peak arises primarily from large-angle Compton interactions in low- Z structural materials, whereas high- Z environments effectively suppress this contribution. The isolated backscatter extractions further revealed characteristic material-dependent signatures—such as the left-hand shoulder in ^{137}Cs and the composite multi-line structure in ^{133}Ba —that align with the expected sensitivity to scattering depth and emission complexity.

A quantitative assessment of detection efficiency and backscatter yield reinforced these observations: replacing lead with copper roughly doubled the overall detection efficiency and increased the number of backscattered photons by more than an order of magnitude in several cases. These trends validate both the interaction physics implemented in the transport kernel and the importance of explicitly modeling the surrounding materials when interpreting measured spectra.

Finally, the controlled variation of the source emission modes showed that isotropic and hemispherical sampling produce consistent spectral shapes, while

the artificially collimated fixed mode suppresses the formation of a well-defined backscatter peak despite its extremely high detection rate. This confirms that the model correctly identifies the geometric conditions under which backscatter is enhanced or suppressed, and highlights the usefulness of directional modes as diagnostic tools for validating transport behavior.

Overall, the results demonstrate that GammaSpectra-MC provides a reliable, interpretable, and computationally efficient framework for reproducing gamma-ray spectra in laboratory settings. Its modular structure makes it well suited for future extensions, including mixed-material shielding, alternative detector types, and higher-energy physics such as pair production, thus offering a flexible platform for both educational applications and hypothesis-driven research in radiation detection.

CODE AVAILABILITY

All simulation scripts, geometry definitions, and post-processing tools are openly available at: <https://github.com/Miguel-Perdomo/gamma-backscatter-montecarlo>

ACKNOWLEDGMENTS

The authors express their gratitude to the Nuclear Physics Group of the Universidad Nacional de Colombia for providing access to the laboratory facilities used in this study. We are especially indebted to Dr. F. Cristancho for his invaluable discussions, guidance, and insights throughout the development of this work. We also thank S. Posada for kindly providing the experimental spectra that supported the validation of the simulation framework.

-
- [1] G. F. Knoll, *Radiation Detection and Measurement* (John Wiley & Sons, New York, 2010).
 - [2] W. R. Leo, *Techniques for Nuclear and Particle Physics Experiments: A How-to Approach* (Springer, Berlin, Heidelberg, 1994).
 - [3] S. H. Hie, A method for synthesizing response functions of NaI detectors to gamma rays, *Nuclear Instruments and Methods* **155**, 475 (1978).
 - [4] D. Flechas *et al.*, The simulation of an imaging gamma-ray Compton backscattering device using Geant4, *International Journal of Modern Physics: Conference Series* **27**, 1460152 (2014).
 - [5] D. Flechas *et al.*, Technical applications of an imaging gamma-ray Compton backscattering device and simulation using GEANT4, in *Proceedings of the 10th Latin American Symposium on Nuclear Physics and Applications (PoS X LASNPA)* (Sissa Medialab, Montevideo, Uruguay, 2014) p. 058.
 - [6] S. Agostinelli *et al.*, Geant4: A simulation toolkit, *Nuclear Instruments and Methods in Physics Research A* **506**, 250 (2003).
 - [7] J. Allison *et al.*, Recent developments in Geant4, *Nuclear Instruments and Methods in Physics Research A* **835**, 186 (2016).
 - [8] R. Wirawan, A. Waris, M. Djamal, H. Gunawan, and H. Kim, Monte Carlo modeling of gamma ray backscattering for crack identification in the aluminum alloy plate, *J. Phys.: Conf. Ser.* **799**, 012010 (2017).
 - [9] A. O. G. Iori and E. M. Boldo, Monte Carlo FLUKA simulation of gamma backscattering for rebar detection in reinforced concrete with basaltic aggregates, *Atoms* **13**, 67 (2025).
 - [10] A. Ryczkowski, M. Kruszyna-Mochalska, B. Pawałowski, G. Bielecka, A. Jodda, P. Adrich, and T. Piotrowski, Shielding disc backscatter calculations in intraoperative radiotherapy using a Monte Carlo simulation based on the method of energy spectra reconstruction, *Sci Rep* **15**, 12431 (2025).
 - [11] A. Aydin, Energy distributions of multiple backscattered photons in materials, *Nuclear Science and Technology* **29**, 23 (2018).
 - [12] U. Akar Tarim *et al.*, Monte Carlo modelling of single and multiple Compton scattering profiles in a concrete material, *Radiation Physics and Chemistry* **85**, 12 (2013).
 - [13] Y.-H. Zuo, J.-H. Zhu, and P. Shang, Monte Carlo simulation of reflection effects of multi-element materials on gamma rays, *Nuclear Science and Technology* **32**, 10 (2021).
 - [14] A. Nikrah, P. Taherparvar, and A. Sadremomtaz, A Monte Carlo simulation of gamma-ray backscattering from concrete shields coated with nanoparticle layers, *Sci Rep* **15**, 29825 (2025).
 - [15] J. H. Hubbell, W. J. Veigele, E. A. Briggs, R. T. Brown, D. T. Cromer, and R. J. Howerton, Atomic form factors, incoherent scattering functions, and photon scattering cross sections, *Journal of Physical and Chemical Reference Data* **4**, 471 (1975).
 - [16] M. J. Berger, J. H. Hubbell, S. M. Seltzer, J. Chang, J. S. Coursey, R. Sukumar, D. S. Zucker, and K. Olsen, *XCOM: Photon cross sections database*, NIST Standard Reference Database 8 (XGAM) (2010).
 - [17] O. Klein and Y. Nishina, Über die streuung von strahlung durch freie elektronen nach der neuen relativistischen quantendynamik von Dirac, *Zeitschrift für Physik* **52**, 853 (1929).
 - [18] R. Friedberg, *Translation and commentary on Rodrigues' "des lois géométriques..."* (2022), arXiv:2211.07787.
 - [19] R. M. Murray, Z. Li, and S. S. Sastry, *A Mathematical Introduction to Robotic Manipulation* (CRC Press, 2017).
 - [20] I. Lux and L. Koblinger, *Monte Carlo Particle Transport Methods* (CRC Press, Boca Raton, 1991).
 - [21] Brookhaven National Laboratory, *NuDat 3.0: National nuclear data center* (2025).
 - [22] W. Jakob *et al.*, *pybind11: Seamless operability between C++11 and Python* (2017).